ARL-TR-9298 • Oct 2021

Assimilating Global Synthetic Weather Radar in the Weather Research and Forecasting Model over Kwajalein Atoll

by Brian P Reen, Huaqing Cai, John W Raby, and James J Ramsey

NOTICES

Disclaimers

The findings in this report are not to be construed as an official Department of the Army position unless so designated by other authorized documents.

Citation of manufacturer's or trade names does not constitute an official endorsement or approval of the use thereof.

Destroy this report when it is no longer needed. Do not return it to the originator.

ARL-TR-9298 ● Oct 2021

Assimilating Global Synthetic Weather Radar in the Weather Research and Forecasting Model over Kwajalein Atoll

Brian P Reen, Huaqing Cai, John W Raby, and James J Ramsey
Computational and Information Sciences Directorate,
DEVCOM Army Research Laboratory

REPORT DOCUMENTATION PAGE

Form Approved
OMB No. 0704-0188

1. REPORT DATE *(DD-MM-YYYY)*	2. REPORT TYPE	3. DATES COVERED (From - To)
October 2021	Technical Report	09/2020–05/2021

4. TITLE AND SUBTITLE
Assimilating Global Synthetic Weather Radar in the Weather Research and Forecasting Model over Kwajalein Atoll

5a. CONTRACT NUMBER

5b. GRANT NUMBER

5c. PROGRAM ELEMENT NUMBER

6. AUTHOR(S)
Brian P Reen, Huaqing Cai, John W Raby, and James J Ramsey

5d. PROJECT NUMBER

5e. TASK NUMBER

5f. WORK UNIT NUMBER

7. PERFORMING ORGANIZATION NAME(S) AND ADDRESS(ES)
DEVCOM Army Research Laboratory
ATTN: FCDD-RLC-EM
2800 Powder Mill Road
Adelphi, MD 20783

8. PERFORMING ORGANIZATION REPORT NUMBER
ARL-TR-9298

9. SPONSORING/MONITORING AGENCY NAME(S) AND ADDRESS(ES)
Office of the Under Secretary of Defense,
Research and Engineering (USD(R&E))
3030 Defense, Pentagon
Washington, DC 20301

10. SPONSOR/MONITOR'S ACRONYM(S)

11. SPONSOR/MONITOR'S REPORT NUMBER(S)

12. DISTRIBUTION/AVAILABILITY STATEMENT
Approved for public release: distribution unlimited.

13. SUPPLEMENTARY NOTES
ORCID IDs: Brian Reen, 0000-0002-2031-4731; Huaqing Cai, 0000-0003-3918-4153

14. ABSTRACT
Global Synthetic Weather Radar (GSWR) data were assimilated into the Weather Research and Forecasting model to determine which assimilation methodology performs best and the difference in performance between a 1-km and a 3-km horizontal grid-spacing configuration. An evaluation of six GSWR assimilation methodologies on a 1-km domain over three case days was used to determine two methodologies that were applied to four additional case days; the two methodologies were also applied on a 3-km domain for all seven case days. The seven case days were used to choose a GSWR assimilation methodology for future use and to determine that for the verification metrics used, the 1-km and 3-km domains perform similarly. Based on this result and that the 1-km domain was approximately nine times slower to run, the 3-km domain will be used in future work to allow more frequently updated forecasts and quicker forecast availability. Use of GSWR is shown to improve the 0-h forecast column maximum reflectivity when convection is sufficiently large to be resolved by GSWR. Higher-resolution observation sources, such as satellite-derived data, should be pursued in the future to improve forecasts of small-scale convection.

15. SUBJECT TERMS
assimilation, Global Synthetic Weather Radar, numerical weather prediction, Weather Research and Forecasting model

16. SECURITY CLASSIFICATION OF:			17. LIMITATION OF ABSTRACT	18. NUMBER OF PAGES	19a. NAME OF RESPONSIBLE PERSON
a. REPORT	b. ABSTRACT	c. THIS PAGE			Brian Reen
Unclassified	Unclassified	Unclassified	UU	41	19b. TELEPHONE NUMBER (Include area code) 301-394-3072

Contents

List of Figures

List of Tables

Acknowledgments

The Office of the Secretary of Defense (OSD) provided funding that helped support the research described in this technical report. Haig Iskenderian (Massachusetts Institute of Technology–Lincoln Laboratory) provided sample Global Synthetic Weather Radar data for use in this investigation. Shawn Ericson and Mariana Scott (Lockheed Martin) provided assistance including guidance regarding the operational context for this research.

The Model Evaluation Tools (MET) package was used for verification. MET was developed by the National Center for Atmospheric Research (NCAR) through grants from the US Air Force Weather Agency and National Oceanic and Atmospheric Administration. This study was made possible in part due to the data made available to the National Oceanic and Atmospheric Administration by various data providers for inclusion in the Meteorological Assimilation Data Ingest System (MADIS). The NCAR Command Language was used for creating some of the graphics in this report (http://dx.doi.org/10.5065/D6WD3XH5). This work was supported in part by high-performance computer time and resources from the Department of Defense High Performance Computing Modernization Program.

1. Introduction

While weather radar provides valuable information for assimilation into numerical weather prediction (NWP) models, it is only available over a relatively small portion of the earth. Weather radar provides a high temporal and spatial resolution data set of an important meteorological phenomenon, namely precipitation. Assimilation of weather radar data into NWP models has been shown to improve short-term forecasts of moist convection, which has led to its assimilation in operational NWP models including the Rapid Refresh (Benjamin et al. 2016) and High-Resolution Rapid Refresh (Alexander et al. 2017) models run operationally by the US National Weather Service. Since weather radar is only available over certain parts of the earth, in order to have a data set with near-global coverage one must rely on satellite-based observations. A variety of meteorological satellites exist that vary in the parts of the earth for which they provide data, how frequently they provide data for a given location, the horizontal resolution of the data they provide, what information they provide on vertical variation, and what fields they observe. None of the extant satellite data provide observations with the combination of equivalent horizontal, vertical, and temporal resolution of the fields provided by radar.

Given the variety of meteorological satellite data available and that it differs from ground-based radar data, it is challenging to directly replace radar observations with satellite observations for purposes of assimilation in NWP models. However, the Massachusetts Institute of Technology–Lincoln Laboratory (MIT-LL) has developed a product called Global Synthetic Weather Radar (GSWR; Veillette et al. 2020) that uses machine learning to process satellite data to create fields normally provided by radar data.

Reen et al. (2020) described the assimilation of GSWR in the Advanced Research version of the Weather Research and Forecasting model (WRF-ARW; Skamarock et al. 2019) using techniques used to assimilate weather radar data in Reen et al. (2019). Here, we enhance the technique used in Reen et al. (2020) to assimilate GSWR to increase the value provided by assimilating GSWR in WRF-ARW. Also, whereas Reen et al. (2020) evaluated the forecasts against GSWR—since the goal was to ascertain how well the information provided by GSWR could be assimilated and no radar observations were available over the areas being assimilated—here we evaluate the forecasts against radar data. This provides a better measure of the improvements gained by assimilating GSWR because radar data provide a more direct (and thus more trustworthy) measurement of reflectivity and are at higher resolution. Finally, to investigate how to best use GSWR in a computing-constrained environment (as is likely to occur for operational implementations of

GSWR assimilation) this study expands the analysis to evaluate the impact on accuracy of decreasing WRF-ARW resolution. Given that this study is closely related to the earlier work described in Reen et al. (2020) some of the descriptions here will be very similar to those provided in that report.

2. Methodology

2.1 GSWR

The GSWR product developed by MIT-LL is an extension of the Offshore Precipitation Capability (Veillette et al. 2018), which covered areas near the continental United States for the Federal Aviation Administration, to near global coverage (Veillette et al. 2020). The only areas GSWR does not cover are the polar regions (it covers 67 S to 67 N at all longitudes but provides data somewhat closer to the poles at some longitudes). GSWR uses machine learning with a convolutional neural network to estimate fields normally provided by radar even where radar data are not available. One input data source is satellites including the Japanese satellite Himawari-8, the European satellites Meteosat-8 and Meteosat-11, and the US Geostationary Operational Environment Satellite (GOES) satellites GOES-16 and GOES-17. Another input data source is lightning data from the Vaisala Global Lightning Dataset 360. NWP output from the US Air Force Global Air-Land Weather Exploitation Model is also used. Space-based radar is used as truth in developing GSWR, namely NASA's Global Precipitation Measurement satellite's Dual-frequency Precipitation Radar.

GSWR provides estimates of column maximum reflectivity (CMR), echo tops, and vertically integrated liquid. GSWR data are available four times per hour and data were assigned to the nearest 15-min time for assimilation in WRF. GSWR is provided at 5-km horizontal grid spacing.

2.2 WRF

WRF-ARW V4.1.2 (Skamarock et al. 2019) was executed in this study as part of the Weather Running Estimate–Nowcast Realtime system (WREN_RT; Reen and Dawson 2018). Subsequent to the research reported in Reen et al. (2020), the ability to assimilate GSWR data was implemented into WREN_RT; this improved the efficiency with which GSWR assimilation could be carried out. WRF-ARW is often referred to as simply WRF, and so WRF will be used for the remainder of this report.

Two WRF configurations were applied in this study, one using nested 9-, 3-, and 1-km horizontal grid-spacing domains (referred to subsequently as the Detailed configuration) and the other using nested 9- and 3-km horizontal grid-spacing domains (referred to subsequently as the Fast configuration). The second configuration runs much more quickly when computational capabilities are limited, allowing for a more timely forecast. The placement of the domains is shown in Fig. 1 for the Detailed configuration and Fig. 2 for the Fast configuration. Both configurations are focused on the Kwajalein Atoll (Republic of the Marshall Islands) region in the Pacific Ocean. In addition to the second configuration lacking a 1-km domain, the sizes of the other two domains differ between the two configurations as does the number of vertical levels and the length of the timesteps used in integrating forward the model solution. A summary of the differences is shown in Table 1. The total number of grid-cell timestep integrations is approximately 15.5 times as many for the Detailed configuration than the Fast configuration as a very rough estimation of the potential timing differences is expected between the two configurations. When running these configurations the WRF runtime for the Detailed configuration was actually approximately 9 times as long as for the Fast configuration.

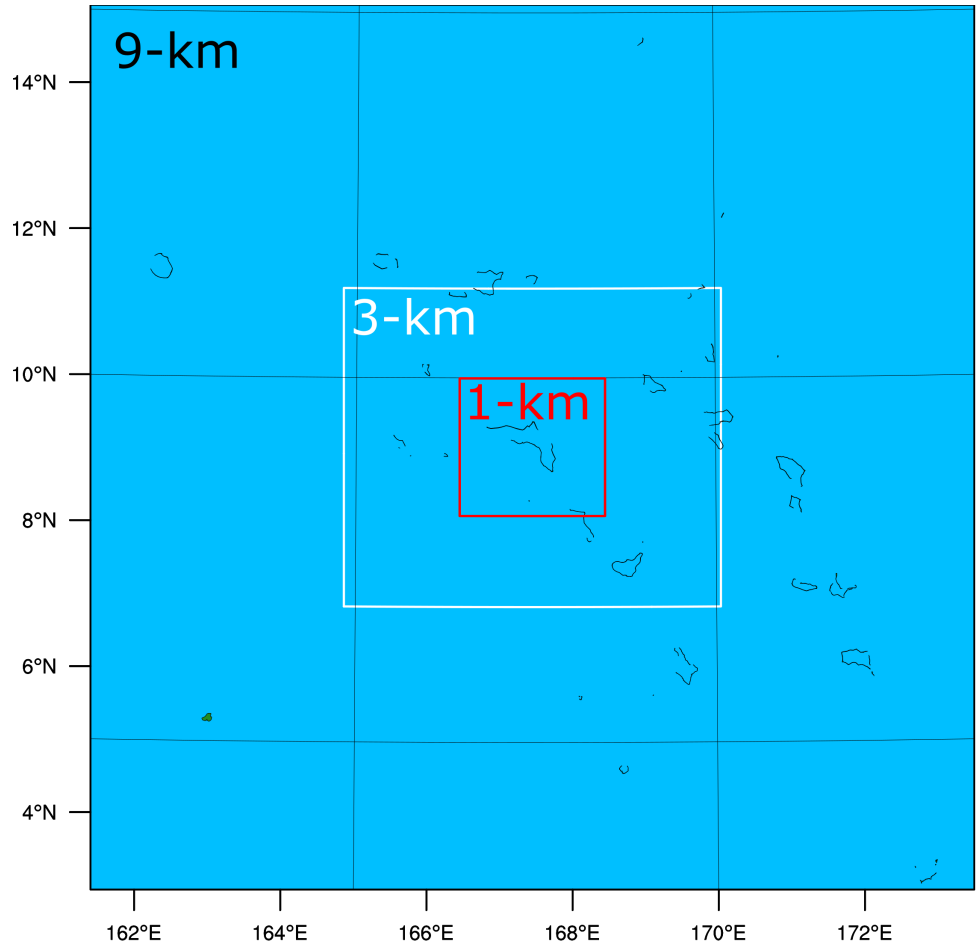

Fig. 1 Map showing coverage of three domains (9-, 3-, and 1-km horizontal grid spacing) of the Detailed configuration, centered over Kwajalein Atoll

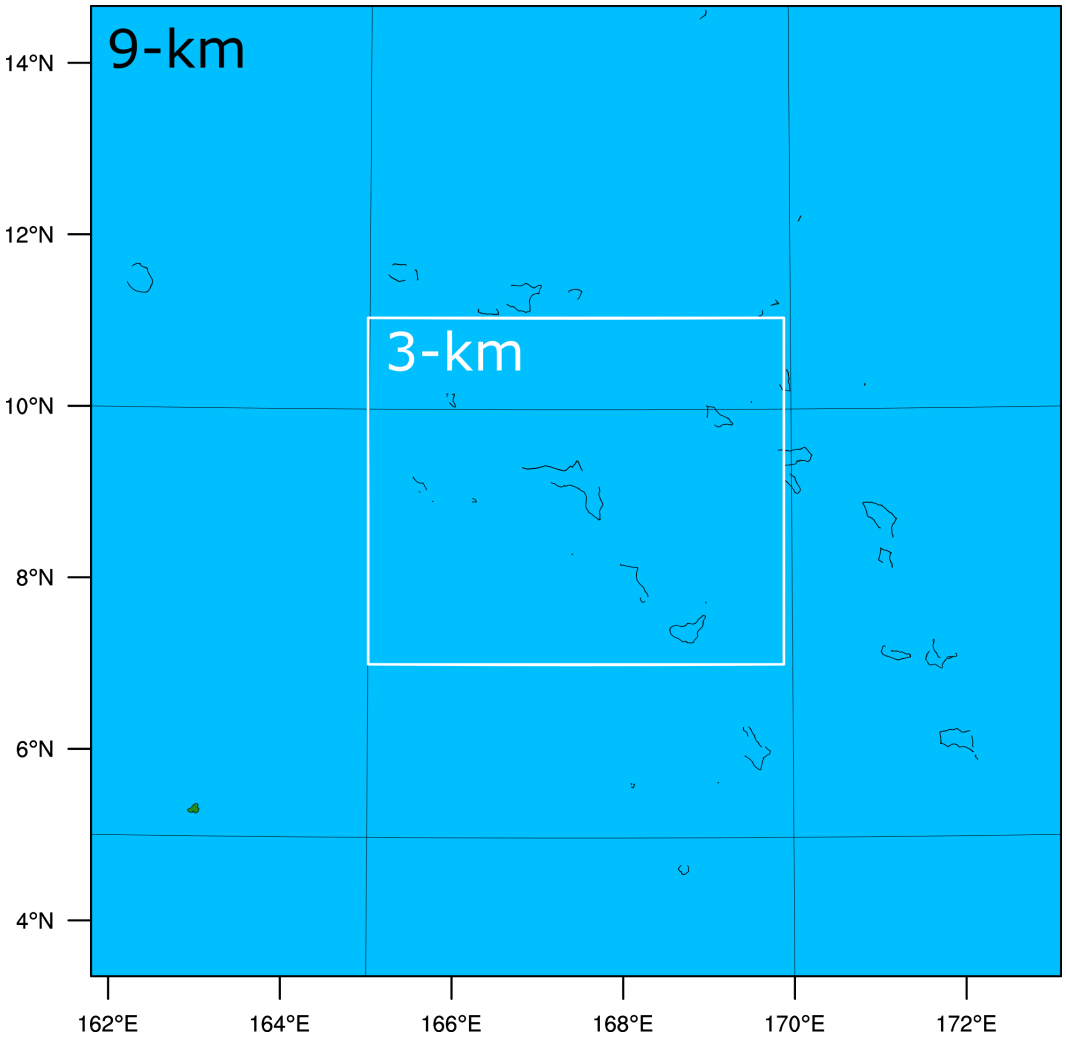

Fig. 2 **Map showing coverage of three domains (9- and 3-km horizontal grid spacing) of the Fast configuration, centered over Kwajalein Atoll**

Table 1 **Comparison of Detailed configuration with 9-, 3-, and 1-km horizontal grid-spacing domains and Fast configuration with 9- and 3-km domains**

Parameter dx (km)	Configuration				
	Detailed			Fast	
	9	3	1	9	3
nx	151	193	223	141	181
ny	151	163	211	141	151
nz	57	57	57	40	40
dt (s)	36	12	4	54	27

For both configurations, the first guess for initial conditions is created from 0.25° horizontal-grid-spacing Global Forecast System (GFS) NWP output (NCEP 2015).

Satellite wind, aircraft, and radiosonde observations obtained from Meteorological Assimilation Data Ingest System (MADIS; https://madis.noaa.gov) are then analyzed onto the GFS data via a multiscan Cressman analysis using the WRF preprocessor Obsgrid. The analysis is carried out on domains larger than the domains used in WRF to allow observations outside the domain to be included in the analysis. Additionally, sea-surface temperature was obtained from the National Centers for Environmental Prediction's Realtime Global (RTG) sea-surface temperature-lookalike product generated from the Near-Surface Sea Temperature (NSST) analysis. The RTG-lookalike NSST files contain NSST analyses that are created in the same format as RTG SST to minimize disruption to users when RTG ceased production.

Both configurations used the same parameterizations. The Yonsei University planetary boundary-layer parameterization (Hong et al. 2006; better known as the YSU scheme) is used and so is the revised Pennsylvania State University–National Center for Atmospheric Research (NCAR) Mesoscale Model version 5 (MM5) surface-layer parameterization (Jimenez et al. 2012). The Noah land-surface model is used (Tewari et al. 2004) although over this oceanic domain should have little effect. Both longwave and shortwave radiation are parameterized via the Rapid Radiative Transfer Model for General circulation models scheme (Iacono et al. 2008), which is better known as the RRTMG scheme. Microphysics are represented by the WSM6 scheme (WRF Single-Moment 6-class; Hong and Lim 2006). The new Tiedtke (Zhang and Wang 2017) cumulus parameterization was used only on the 9-km domain. This is so that on the finer domains where deep convection is better resolved (e.g., the 3-km and 1-km domains) we do not represent the deep convection both explicitly and via the parameterization and thus represent the same convection twice and double-count its effects. The choice of parameterizations matches that used in Reen et al. (2019) and matches the WRF tropical configuration except that we apply the revised MM5 surface-layer scheme. The parameterizations used do not match those in Reen et al. (2020) as that study was not over oceanic tropical regions.

2.3 Assimilation Methodology

The methodology used to assimilate GSWR in this study is built on the methodology to assimilate GSWR described in Reen et al. (2020) that was adapted from the methodology used to assimilate radar data in Reen et al. (2019) (which itself was based on the methodology used to assimilate radar data in the High Resolution Rapid Refresh model). The method applied involves creating heating profiles based on GSWR and applying these heating profiles in WRF to initiate, enhance, or suppress modeled convection.

2.3.1 Calculating Reflectivity Profile

At each gridpoint the GSWR CMR ($GSWR_{CMR}$) and reference reflectivity profiles from the data-assimilation program Gridpoint Statistical Interpolation (GSI; Shao et al. 2016) are used to create reflectivity profiles (A_{ref}). In GSI the reference profiles are used to extend profiles above the top of the radar data, whereas here we create entire profiles using the reference profiles based on $GSWR_{CMR}$. While GSI V3.6 has summer and winter reference profiles, it is hard-coded to use the summer profiles and so those are used here. The GSI reference profiles each range from 0.0 to 1.0 and one multiplies the profile by CMR to create the actual profile. GSI has reference profiles for CMR from 20 to 50 dBZ in 5-dBZ increments; we use the 20-dBZ profile for CMR less than 20 dBZ and the 50-dBZ profile for CMR greater than 50 dBZ.*

While in Reen et al. (2020) GSWR echo top ($GSWR_{ET}$) was not used, here the echo top is used to adjust the reflectivity profile that was created by combining $GSWR_{CMR}$ and the GSI reference profiles (i.e., A_{ref}). Above $GSWR_{ET}$ the A_{ref} is limited to being no greater than 10 dBZ. Between the height of $GSWR_{CMR}$ and $GSWR_{ET}$, A_{ref} is adjusted to be no less than 18 dBZ (the reflectivity threshold used to define $GSWR_{ET}$). If this process results in A_{CMR} being less than $GSWR_{CMR}$ then at all heights below $GSWR_{ET}$ the quantity $GSWR_{CMR} - A_{CMR}$ is added to A_{ref} so that $A_{CMR} = GSWR_{CMR}$ (i.e., the reflectivity profile created has the same CMR as GSWR).

This technique to create a reflectivity profile A_{ref} from $GSWR_{CMR}$, $GSWR_{ET}$, and reference profiles assumes that convection with a given CMR always has the same vertical profile, whereas it could be beneficial to incorporate case-specific details in the vertical profile. WRF will create a reflectivity profile consistent with its understanding of the case-specific meteorology, and so it is better to strengthen or weaken the WRF reflectivity profile rather than impose an assumed vertical profile. Therefore, where WRF provides sufficiently strong convection we use the WRF reflectivity profile (WRF_{ref}) to create an alternative reflectivity profile (B_{ref}) for use in calculating the heating to apply in WRF. Specifically, instead of using the GSI reference profile we scale the WRF reflectivity profile as follows: $B_{ref} = WRF_{ref} * (GSWR_{CMR}/WRF_{CMR})$. If WRF_{CMR} is too small compared with $GSWR_{CMR}$, then scaling WRF_{ref} is unlikely to create a realistic profile. Thus, this technique is only used if $WRF_{CMR} >= 0.5 * GSWR_{CMR}$. Therefore:

$$GSWR_{ref} = A_{ref} \; if \; WRF_{CMR} < 0.5 * GSWR_{CMR}$$

$$GSWR_{ref} = B_{ref} \; if \; WRF_{CMR} \geq 0.5 * GSWR_{CMR}$$

* dBZ = decibel relative to reflectivity factor Z.

2.3.2 Calculating Reflectivity-Derived Latent Heating

Reflectivity-derived latent heating (RDLH) is then calculated from $GSWR_{ref}$ as described in Reen et al. (2020). First, the reflectivity factor is used to estimate the rain/snow condensate *(f[Z_e])* it represents as follows:

$$f[Z_e] = \frac{1.5}{264083} * 10^{(Z/17.8)}, \quad (1)$$

where

Z = radar reflectivity

Then RDLH was calculated as

$$\text{RDLH} = \left(\frac{d\theta}{dt}\right)_{LH} = \left(\frac{1000}{p}\right)^{R_d/c_p} * \frac{(L_v+L_f)(f[Z_e])}{t_c c_p}, \quad (2)$$

where

p = pressure (hPa)

R_d = dry gas constant (≈287.059)

c_p = specific heat of dry air at constant p (≈1004.705 J kg^{-1} K^{-1}) — R_d/c_p is 1/3.5

L_v = latent heat of vaporization at 0° C (2.501E6 J kg^{-1})

L_f = latent heat of fusion at 0° C (0.3335E6 J kg^{-1})

t_c = time period of condensate formation (in seconds, here set to 15*60)

θ = potential temperature

t = time

LH = latent heating

f[Z_e] = reflectivity factor converted to rain/snow condensate

As in Reen et al. (2020) RDLH is set to zero if $GSWR_{ref}$ < 5 dBZ since in the past tests GSWR sometimes reported widespread low dBZ that did not appear to be realistic. An entire column of RDLH is set to zero if horizontal smoothing of RDLH results in no layer in that column having RDLH > 0.00002 Ks^{-1}. RDLH is not preemptively set to zero within the atmospheric boundary layer in this study.

As reported in Reen et al. (2020), sudden imposition of large RDLH could be problematic and so we here apply the same adjustment described in that study to $GSWR_{ref}$:

$$GSWR_{ref} = \min\left(\max\left[WRF_{ref} + 10{,}40\right], GSWR_{ref}\right)$$

This allows large RDLH stemming from large $GSWR_{ref}$ to be gradually introduced and minimize noise caused by its imposition.

2.3.3 Applying RDLH

The RDLH can affect WRF simulations in five ways:

1. By replacing the microphysics heating term (MPHT) calculated by the microphysics parameterization.
2. By determining whether the cumulus parameterization heating term (CPHT) calculated by the cumulus parameterization is applied. If RDLH is non-negligible ($\geq 1.0 * 10^{-7}$ Ks^{-1}), then CPHT is not applied. This is relevant only to the 9-km domain since that is the only domain using a cumulus parameterization.
3. By altering a variable in certain cumulus parameterization schemes. This is not relevant to the cumulus parameterization used in this study (the new Tiedtke scheme, which is only used on the 9-km domain).
4. By modifying the prevalence of hydrometeors. If RDLH = 0, then at each timestep the mixing ratio of rain, snow, graupel, and hail is decreased by the amount that would result in a 0 g kg^{-1} mixing ratio in 1 h if there were no other tendency terms.
5. By modifying the prevalence of cloud water mixing ratio. If RDLH=0, then at each time step the mixing ratio of cloud water is decreased by the amount that would result in a 10% decrease in 1 h if there were no other tendency terms.

The replacement of the MPHT by RDLH (Item 1 in the list) is the main mechanism by which GSWR is assimilated into WRF. To first order, if RDLH is present (i.e., not missing) then RDLH is used instead of MPHT. Since the observation we are assimilating provides a CMR (and echo top) rather than a full profile, we have lower confidence in the profile we are assimilating than if GSWR provided the full profile. Thus, the technique is modified in light of the lower confidence we have in $GSWR_{ref}$ compared with our confidence in $GSWR_{CMR}$. First, if $GSWR_{CMR}$ indicates the reflectivity in a profile is too strong and application of MPHT would result in a lower heating than RDLH, we apply MPHT since GSWR does not directly indicate how much weaker reflectivity should be at a given height (i.e., if RDLH > 0, $WRF_{CMR} > GSWR_{CMR}$, and MPHT < RDLH, then we apply MPHT). Second, if GSWR indicates the reflectivity in a profile is too weak and application of MPHT would result in a larger heating than RDLH, we apply MPHT since GSWR does

not directly indicate how much stronger reflectivity should be at a given height (i.e., if RDLH > 0, $WRF_{CMR} < GSWR_{CMR}$, and MPHT > RDLH, then we apply MPHT).

Since GSWR is coarser horizontally than some of the WRF domains used in this study, GSWR may indicate that there is no convection in a grid cell only because the convection is smaller than can be resolved by GSWR. Therefore, an option not in Reen et al. (2020) was added to prevent GSWR from suppressing small convective elements. In particular, the user chooses via name-list setting *radar_lh_cmr_min_size_km* a horizontal extent (in km) that is the minimum size of convection that GSWR will be allowed to suppress. The square of WRF model cells most closely matching this horizontal extent and centered on the WRF grid point in question is checked to see if more than 50% of the WRF columns in that box have a CMR greater than 5 dBZ. If they do, then the convection is considered suppressible; otherwise, the convection is deemed to be nonsuppressible and we act as though RDLH is missing at that point and so MPHT is applied. Note that in addition to affecting whether MPHT is applied (Item 1), if the convection is deemed to be nonsuppressible then hydrometeors (Item 4) and cloud–water mixing ratio (Item 5) are not decreased when RDLH = 0.

Another new option added (*radar_lh_no_weaken_nonzero*) prevents RDLH from weakening WRF_{ref} in cases where RDLH indicates nonzero heating due to reflectivity. In particular, if this option is enabled, RDLH is nonzero, and $GSWR_{CMR} < WRF_{CMR}$, then we apply MPHT instead of RDLH. Since the GSWR does not resolve the finer-scale convection structure in high-resolution NWP, we do not want GSWR to smooth this out.

RDLH is applied during a 6-h pre-forecast period. During the 6-h pre-forecast the RDLH field valid at the end of each 15-min period is applied throughout the 15-min period (as illustrated in Fig. 3 for a 1-h preforecast period). The GSWR data are available 4 times per hour and assigned to the nearest 15-min interval to its valid time.

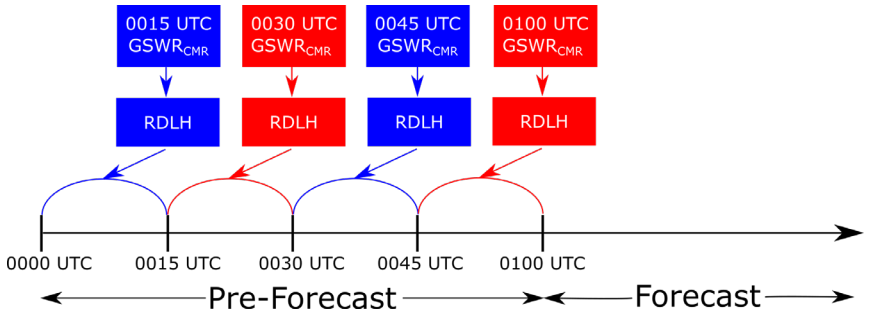

Fig. 3 During the preforecast period the RDLH valid at the end of each 15-min period is applied throughout that 15-min period (although diagram illustrates a 1-h preforecast for clarity, we used a 6-h preforecast)

2.4 Experimental Design

Three case days were simulated using the Detailed configuration and were used to narrow the assimilation methodology to two possible configurations. Next, the best two assimilation-methodology configurations were applied to four additional case days for the Detailed configuration and applied to all seven cases days for the Fast configuration. Assimilation was carried out during a 6-h preforecast that is followed by a 6-h forecast.

The assimilation Methodology A (Table 2) is the control experiment wherein GSWR is not assimilated. However, this experiment still has a 6-h preforecast but instead of being used for assimilation and model spin-up it is used solely for model spin-up. One factor that varies among the other experiments is the minimum horizontal size of areas of reflectivity in which GSWR is permitted to suppress reflectivity (*radar_lh_cmr_min_size_km*) is varied to be 0, 5, or 9 km. The other factor that varies among the experiments is whether GSWR-derived RDLH is prevented from being applied where it is nonzero and is smaller than MPHT (*radar_lh_no_weaken_nonzero*).

Table 2 Details on assimilation methodologies tested, including whether GSWR was assimilated, and values of *radar_lh_cmr_min_size_km* and *radar_lh_no_weaken_nonzero* (in the WRF namelist "Y" is represented as ".true." and "N" as ".false.")

Assim. method	GSWR	*radar_lh_cmr_min_size_km*	*radar_lh_no_weaken_nonzero*
A	N	N/A	N/A
B	Y	0	N
C	Y	5	N
D	Y	9	N
E	Y	0	Y
F	Y	5	Y
G	Y	9	Y

The experiment names (Table 3) include the letter representing the assimilation method applied and the horizontal grid spacing in kilometers of the finest domain in that configuration. The finest domain is the domain that is evaluated and is 1 km in the Detailed configuration and 3 km in the Fast configuration. Table 3 also indicates which experiments were run on which case days.

Table 3 Experiment names created based on assimilation method, whether the Detailed (9-, 3-, or 1-km horizontal grid-spacing domains) or Fast (9- or 3-km domains) configuration was used, and which days each experiment was run (dates are the beginning of the simulation in UTC in the format M/DD where M = month number and DD = day of month)

Exp. name	Assim. method	Config	Dates (UTC)						
			5/15	5/28	6/7	6/10	6/11	6/13	6/19
A1	A	Detailed	Y	Y	Y	Y	Y	Y	Y
B1	B	Detailed	Y	Y	Y	…	…	…	…
C1	C	Detailed	Y	Y	Y	…	…	…	…
D1	D	Detailed	Y	Y	Y	…	…	…	…
E1	E	Detailed	Y	Y	Y	Y	Y	Y	Y
F1	F	Detailed	Y	Y	Y	…	…	…	…
G1	G	Detailed	Y	Y	Y	Y	Y	Y	Y
A3	A	Fast	Y	Y	Y	Y	Y	Y	Y
E3	E	Fast	Y	Y	Y	Y	Y	Y	Y
G3	G	Fast	Y	Y	Y	Y	Y	Y	Y

2.5 Verification Technique

WRF_{CMR} is compared with CMR from weather radar ($radar_{CMR}$) during the 6-h forecast time period to evaluate how well the experiments perform. One metric used in the evaluation is the Fractions Skill Score (FSS; Roberts 2008; Roberts and Lean 2008). FSS is a neighborhood method and it is applied here by comparing every square neighborhood of a given size in the model domain with the coincident neighborhood in the weather-radar data to determine whether a reflectivity exceeding some threshold occurs in either one or both of the neighborhoods. The FSS of CMR indicates how well the model is forecasting the placement of moist convection and FSS is not decreased by errors smaller than the scale of the neighborhood. A perfect score of FSS is 1.0. FSS is evaluated using 10-, 20-, and 30-dBZ thresholds, which means that is evaluating areas with reflectivity greater than these values. Another metric applied here is a measure of the bias obtained by dividing the fraction of the model domain exceeding a certain reflectivity threshold by the fraction of the radar domain exceeding that same reflectivity threshold. This metric will be referred to as bias; a perfect score for bias is 1.0, with a smaller number indicating the model underforecasts coverage of reflectivity for the given threshold and a larger number indicating the model overforecasts coverage of reflectivity at the given threshold.

3. Results

3.1 3-Day Seven-Methodology Comparison

The time series of CMR FSS aggregated over three case days for six GSWR assimilation methodologies and a control experiment without GSWR assimilation

are shown in Fig. 4 for the Detailed WRF configuration. All tested GSWR assimilation methodologies improve the FSS for the first 2 h for all reflectivity thresholds shown (10, 20, and 30 dBZ) and both neighborhood sizes (121 km^2 and 625 km^2) while for the lower two reflectivity thresholds the improvement almost always lasts throughout the 6-h forecast. Neighborhoods with CMR ≥30 dBZ are less frequent than neighborhoods exceeding the lower two thresholds and it will likely be more difficult to forecast where these areas will occur farther into the forecast period compared with areas with lower CMR. The relationship of FSS among the experiments is very similar between the two neighborhood sizes shown although, unsurprisingly, the FSS values are generally higher for the larger neighborhood size. The GSWR assimilation experiments form two clusters in terms of their FSS values based on whether they allow GSWR to weaken model reflectivity in locations where GSWR indicates that there is non-negligible reflectivity (i.e., *radar_lh_no_weaken_nonzero* = Y; Experiments E1, F1, and G1) or not (i.e., *radar_lh_no_weaken_nonzero* = N; Experiments B1, C1, and D1). The *radar_lh_no_weaken_nonzero*=Y cluster has higher FSS than the other cluster for the first approximately 4 h for the 10-dBZ threshold and approximately 2.5 h for the 20-dBZ threshold, while for the 30-dBZ threshold it is generally better at 0.50–1.50 h. Within the cluster producing higher FSS, the experiments differ in the minimum size of convection that is allowed to be suppressed by GSWR when GSWR indicates there is negligible reflectivity (*radar_lh_cmr_min_size_km*). Among this cluster, it is difficult to ascertain which experiment performs best.

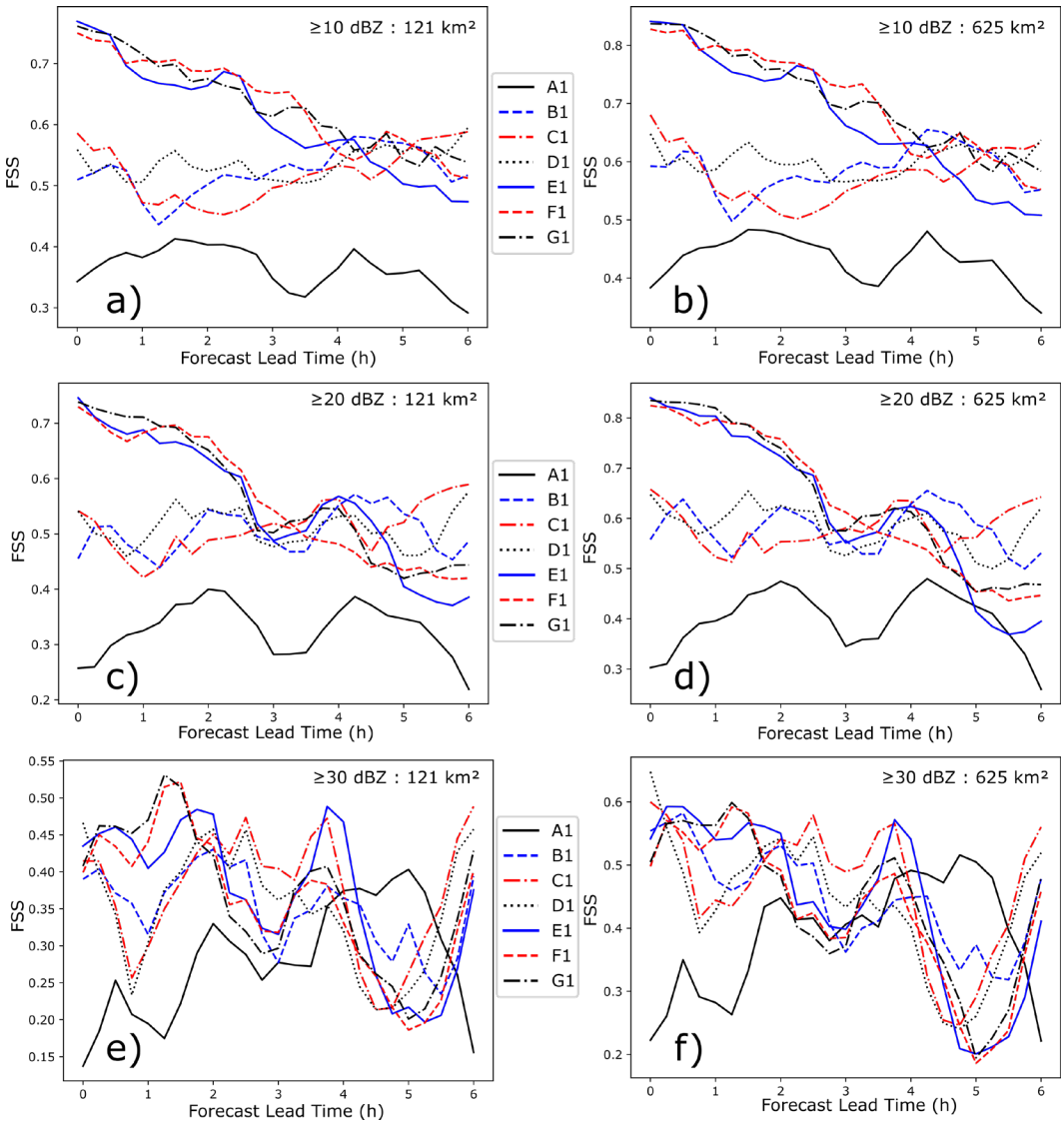

Fig. 4 Time series of CMR FSS on 1-km horizontal grid-spacing domain for seven experiments aggregated over 3 case days for reflectivity thresholds of ≥10 dBZ (a and b), ≥20 dBZ (c and d), and ≥30 dBZ (e and f) for neighborhoods of 11 × 11 = 121 grid cells = 121 km² (a, c, and d) and 25 × 25 = 625 grid cells = 625 km² (b, d, and f)

The CMR-bias time series (Fig. 5) shows the same clustering of experiments seen in CMR FSS (Fig. 4) with the *radar_lh_no_weaken_nonzero*=Y cluster generally having larger values of bias through approximately the first 4 h. For bias the two neighborhood sizes show almost identical results. Without GSWR assimilation (A1) at the 10-dBz and 20-dBz thresholds there is a CMR underforecast bias throughout the forecast that worsens as the forecasts advances, whereas for the 30-dBZ threshold an overforecast bias at the beginning of the forecast period eventually leads to an underforecast bias by the end of the forecast. Assimilation of GSWR with *radar_lh_no_weaken_nonzero* = N (B1, C1, and D1) worsens the

underforecast bias during approximately the first 3 h at the 10-dBZ and 20-dBZ thresholds, while introducing an underforecast bias at the 30-dBz threshold. Toward the end of the forecast period, the *radar_lh_no_weaken_nonzero*=N cluster decreases the underforecast bias compared with the no-GSWR assimilation experiment, particularly for the 10-dBZ threshold. Unlike the *radar_lh_no_weaken_nonzero*=N cluster, the other cluster (*radar_lh_no_weaken_nonzero* = Y; E1, F1, and G1) has a higher bias value than the experiment without GSWR assimilation (A1). This improves the underforecast bias at 10- and 20-dBZ thresholds but leads to an overforecast bias for the 30-dBZ threshold for the first 3.5 h.

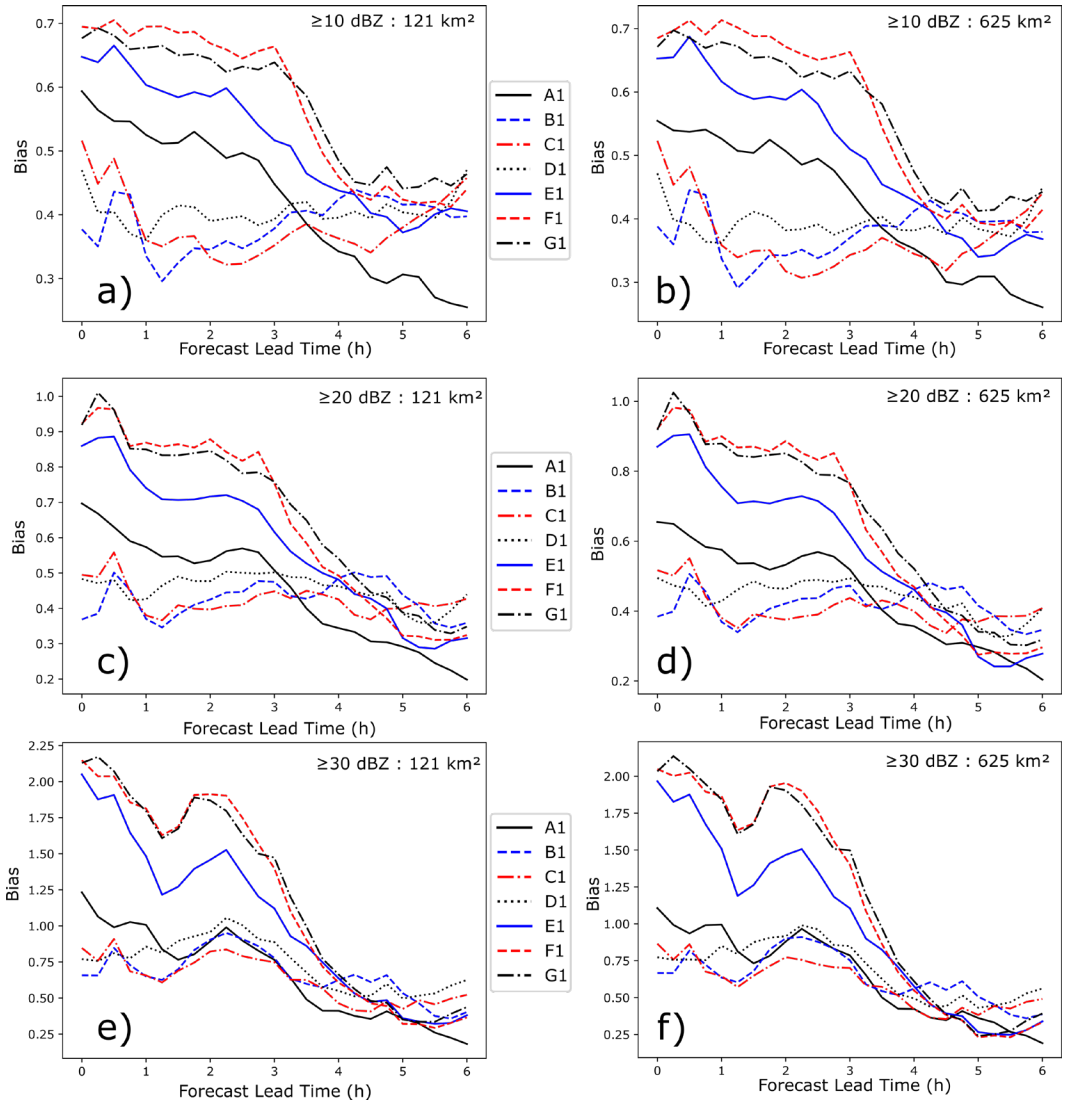

Fig. 5 Time series of CMR bias on 1-km horizontal grid-spacing domain for 7 experiments aggregated over 3 case days for reflectivity thresholds of ≥10 dBZ (a and b), ≥20 dBZ (c and d), and ≥30 dBZ (e and f) for neighborhoods of 11 × 11 = 121 grid cells = 121 km² (a, c, and d) and 25 × 25 = 625 grid cells = 625 km² (b, d, and f)

Since the *radar_lh_no_weaken_nonzero*=Y cluster (E1, F1, and G1) produces better FSS at all reflectivity thresholds and better bias at the 10- and 20-dBZ thresholds, these experiments are considered for further experimentation. It is more difficult to determine which of these three experiments is best. WRF forecasts used for further testing involve additional case days and a different horizontal grid spacing and so it may be the results found in these three cases at 1-km horizontal grid spacing are not representative of the subsequent testing. Thus, instead of choosing a single GSWR assimilation methodology, two methodologies used in the better-performing cluster were chosen for further use (E and G). Of the three methodologies used in the better-performing cluster, these two represent the extremes (minimum suppressible convection size of 0 km [Method E] and 9 km [Method G]) and so span the solution space for which *radar_lh_cmr_min_size_km* was tested in the three case days.

3.2 7-Day Three-Methodology Comparison

The two GSWR assimilation methodologies chosen from the 3-day test (E and G) and the no-GSWR assimilation methodology (A) are applied to seven case days for both the Detailed and Fast configurations. The seven case days reported here include the three case days used in the 3-day comparison. The goal of analyzing these WRF forecasts is twofold. The first goal is to determine which of the two assimilation methodologies (E or G) performs better to determine which methodology should be used for future work. The second goal is to determine whether the Detailed configuration provides sufficient improvement over the Fast configuration to justify use of the Detailed configuration, given that the Detailed configuration requires significantly more computational resources than the Fast configuration.

The experiments shown here are those without GSWR assimilation (A1 from the Detailed configuration and A3 from the Fast configuration), using GSWR assimilation method E (E1 and E3), and using GSWR assimilation method G (G1 and G3). The results from the Detailed configuration are from the portion of the 1-km horizontal grid-spacing domain for which radar data are available (radar is not available in an area in the northwest corner of the domain). The results from the Fast configuration are for the portion of a 3-km domain that is within the area covered by the portion of the 1-km domain of the Detailed configuration for which radar data are available.

3.2.1 Statistical Comparison of 7-Day Aggregate Performance

The neighborhood sizes used in this section are 225 and 729 km^2. Due to the different horizontal grid spacings of the domains evaluated here, this involves a different numbers of grid cells for the Detailed versus Fast configurations.

Figure 6 shows time series of CMR FSS aggregated over the seven case days for WRF forecasts. The FSS indicates the use of either of the GSWR assimilation methodologies leads to improvements in both of the configurations (Experiments A* without GSWR assimilation vs. Experiments E* and G* with GSWR assimilation where * indicates 1 or 3). The improvement lasts throughout the forecast for the 10-dBZ threshold, to at least 4 h for the 20-dBZ threshold and to at least 3 h for the 30-dBZ threshold. Comparing the two GSWR assimilation methodologies, the results are quite similar, with G (which is used in the G* experiments) potentially slightly better than E (used in the E* experiments). Comparing the Detailed and Fast configuration for the G methodology (i.e., G1 vs. G3) suggests the FSS values of the two experiments are close enough that it is difficult to justify the significantly larger amount of computational expense required for the Detailed configuration (approximately nine times as much).

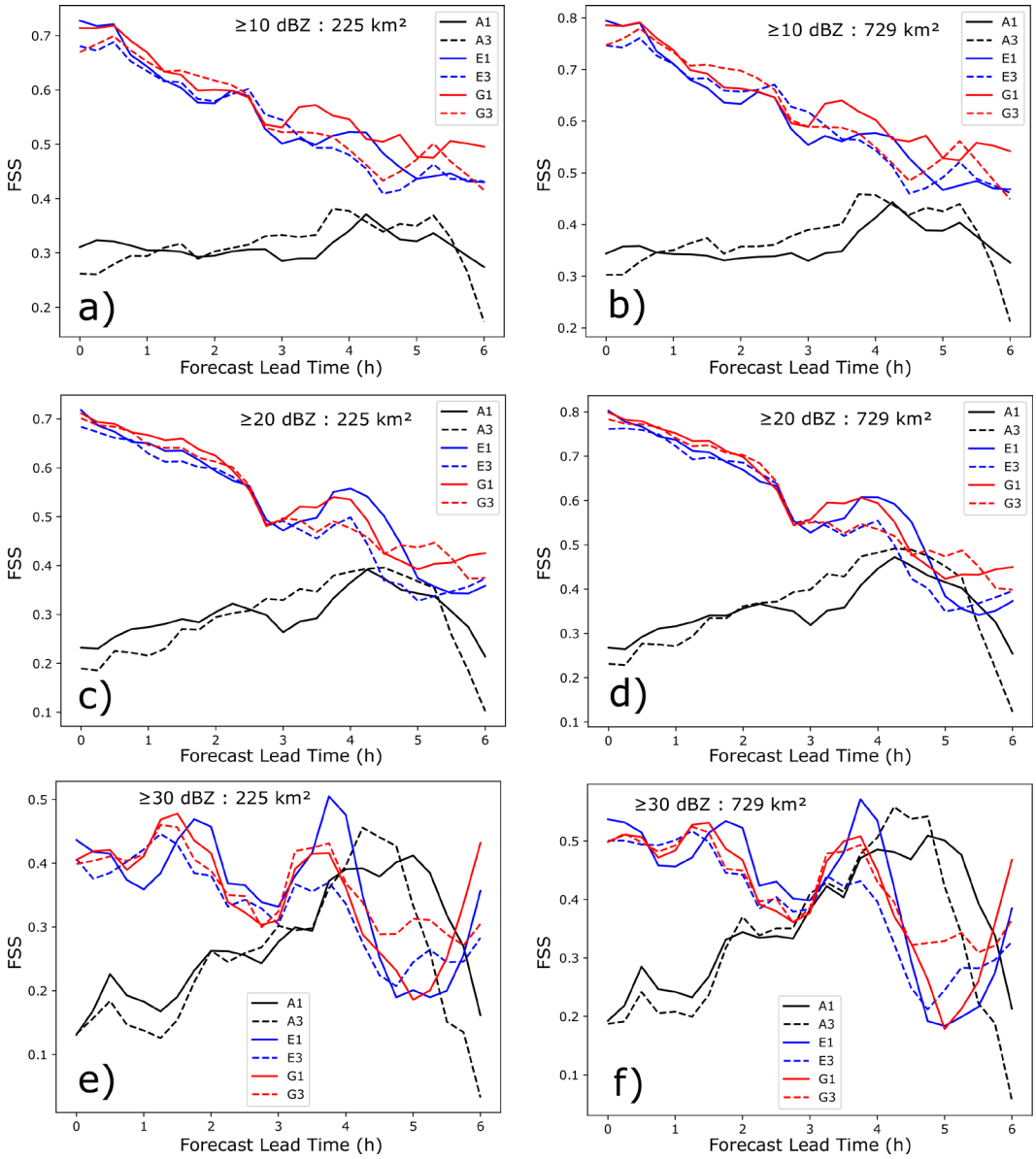

Fig. 6 Time series of CMR FSS for 3 experiments on 1-km (A1, E1, and G1) and 3-km horizontal grid-spacing domain (A3, E3, and G3) aggregated over 7 case days for reflectivity thresholds of ≥10 dBZ (a and b), ≥20 dBZ (c and d), and ≥30 dBZ (e and f) for neighborhoods of 225 km² (a, c, and d) and 729 km² (b, d, and f)

The bias time series for CMR aggregated for the seven case days is shown in Fig. 7. Without GSWR assimilation (A*) there is an underforecast bias throughout the forecast period for both the 10- and 20-dBZ thresholds, whereas for the 30 dBZ there is underforecast bias for Fast configuration for all times and the Detailed configuration for most times. The assimilation of GSWR generally increases the value of bias through the first 3 h, leading to less of an underforecast at the 10- and 20-dBZ thresholds but to an overforecast at the 30-dBZ threshold. Between the E* and G* experiments, G* generally has a higher bias and thus less of an

underprediction at the 10- and 20-dBZ thresholds but more of an overprediction at the 30-dBZ threshold. Since the 10- and 20-dBZ thresholds will be exceeded much more often than the 30-dBZ threshold, it seems that improved bias on the 10- and 20-dBZ thresholds with degraded bias on the 30-dBZ threshold is preferable to the opposite case. Also, it seems better to overwarn than to miss cases with convection. For these reasons, the G assimilation methodology appears better than E in terms of the bias metric. It is unclear whether the Fast or Detailed configuration performs better in terms of bias; thus, this metric provides no justification for using the much more computationally expensive Detailed configuration.

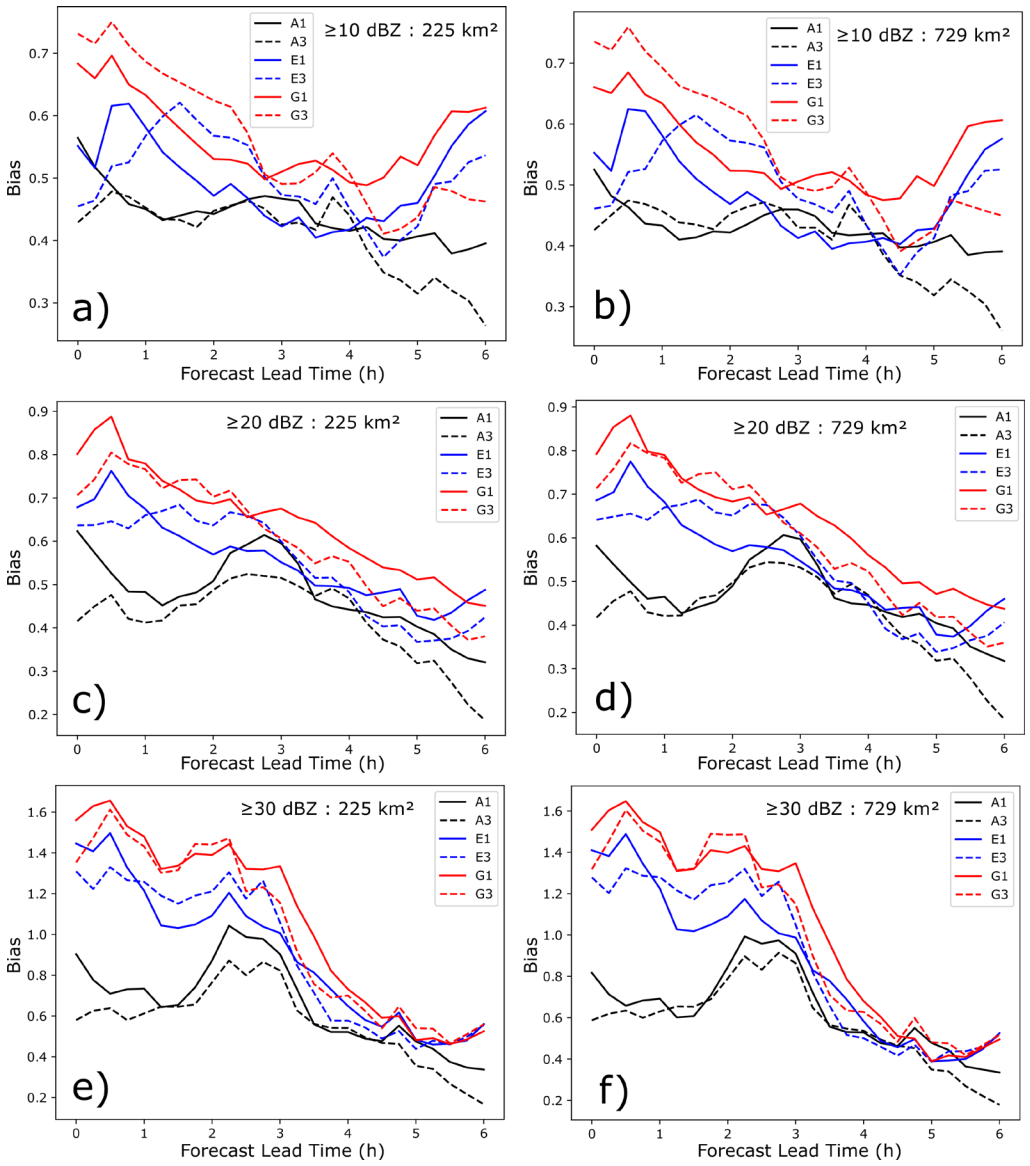

Fig. 7 Time series of CMR bias for 3 experiments on 1-km (A1, E1, and G1) and 3-km horizontal grid-spacing domain (A3, E3, and G3) aggregated over 7 case days for reflectivity thresholds of ≥10 dBZ (a and b), ≥20 dBZ (c and d), and ≥30 dBZ (e and f) for neighborhoods of 225 km² (a, c, and d) and 729 km² (b, d, and f)

This evaluation suggests assimilation methodology G be used with the Fast configuration. The method of evaluation used here does not capture whether the Detailed configuration provides a more realistic vertical structure than the Fast configuration, nor does it address whether the Detailed configuration might better capture fine-scale horizontal features. The evaluation does indicate that for forecasting whether convection will occur in a 15- × 15-km^2 box both configurations perform similarly enough that it may be difficult to justify the increased computational cost of the Detailed configuration.

3.2.2 Individual Case Day 0-h Forecast Comparison

Examining the seven individual case days included in the aggregate statistics can provide insight on how the impact of GSWR varies among case days. Fig. 8–14 show the CMR at the end of the preforecast assimilation period for each of the 7 case days. This allows evaluation of how assimilation of GSWR influenced the accuracy of the initial conditions of the forecast. In each figure, Panel a is the $\text{radar}_{\text{CMR}}$, which is the field against which the WRF forecasts were evaluated, and Panel b is GSWR_{CMR}. Panels c–e show the WRF forecasts from the Detailed configuration (1-km horizontal grid-spacing domain). Panel c is the control experiment without GSWR assimilation (A1), Panel d assimilates GSWR using methodology E (E1), and Panel e assimilates GSWR using methodology G (G1). Panels f–h show the equivalent experiments from the Fast configuration as those in Panels c–e from the Detailed configuration. In Panels f–h, only the portion of the Fast configuration's 3-km domain covered by the 1-km domain of the Detailed configuration is shown.

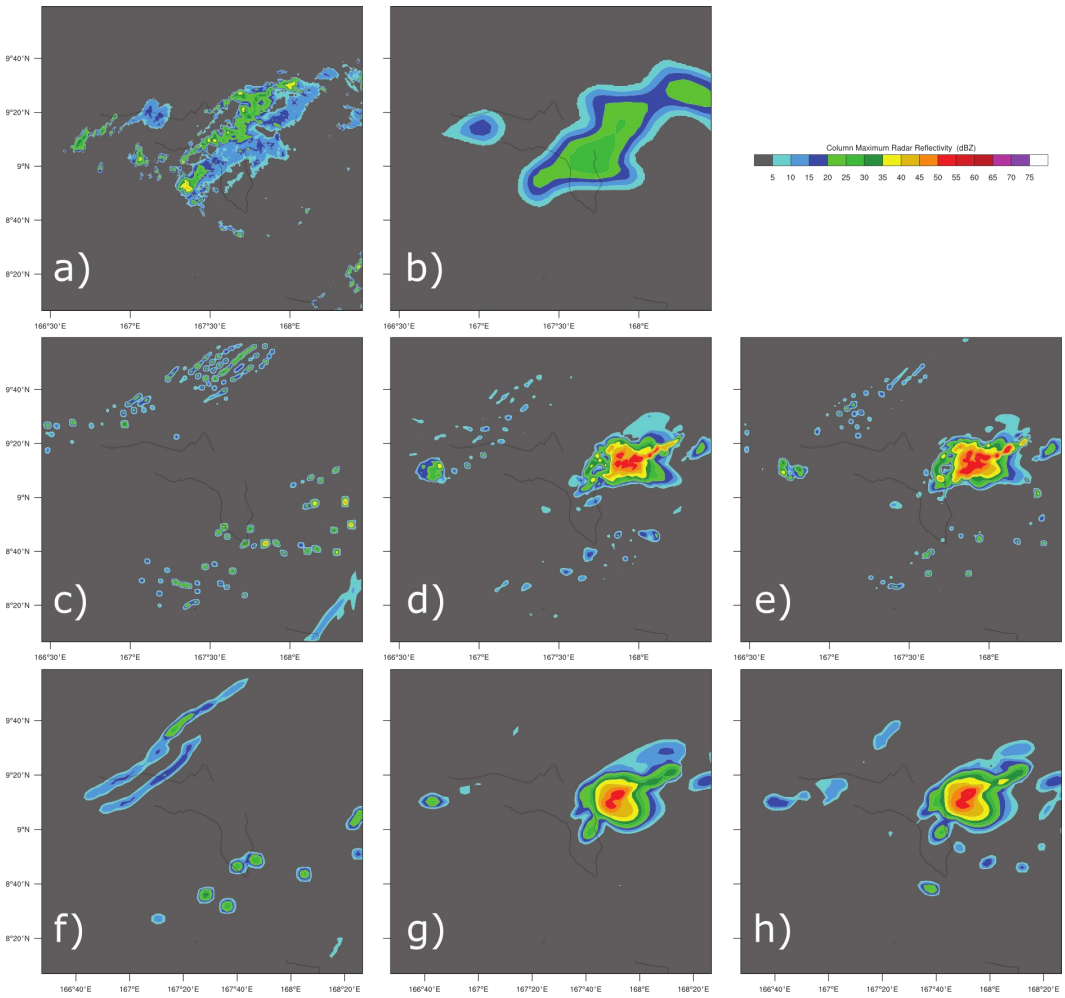

Fig. 8 CMR at end of preforecast (1800 UTC 15 May 2020) from a) radar, b) GSWR, c) A1, d) E1, e) G1, f) A3, g) E3, and h) G3 over area of 1-km domain

For 1800 UTC on 15 May 2020 the GSWR CMR (Fig. 8b) generally appears to be a smoothed version of the radar CMR (Fig. 8a) as would be expected given the coarser resolution of GSWR as compared with the radar data. The control experiments (Fig. 8c and 8f) do not show CMR well correlated with the radar CMR. The assimilation of GSWR by any of the methods (Fig. 8d, e, g, and h) allows the model to reproduce an area of reflectivity within the area where both radar and GSWR indicates there is reflectivity. Assimilation Methodology G (Fig. 8e) allows small areas of convection to be stronger in the 1-km Detailed simulation than Methodology E (Fig. 8d), and in the 3-km Fast simulation allows additional small areas of reflectivity (Fig. 8h vs. 8g). This is consistent with Methodology G requiring areas of convection have a horizontal extent of 9-km before GSWR is allowed to suppress it whereas methodology has no such limit. For both the E and G methodologies the CMR field is smoother for the Fast simulation than the Detailed configuration, which is expected given the 3-km horizontal grid spacing

of the Fast simulation versus the 1-km horizontal grid spacing of the Detailed configuration. More area is covered by high CMR values in the experiments assimilating GSWR than indicated by radar. Overall, GSWR assimilation improves the reflectivity of the 0-h forecast in this case, with at least some of the reason that WRF does not perform better being the mismatch between GSWR and radar data, which in turn is at least partially explained by differences between the GSWR and radar horizontal resolution.

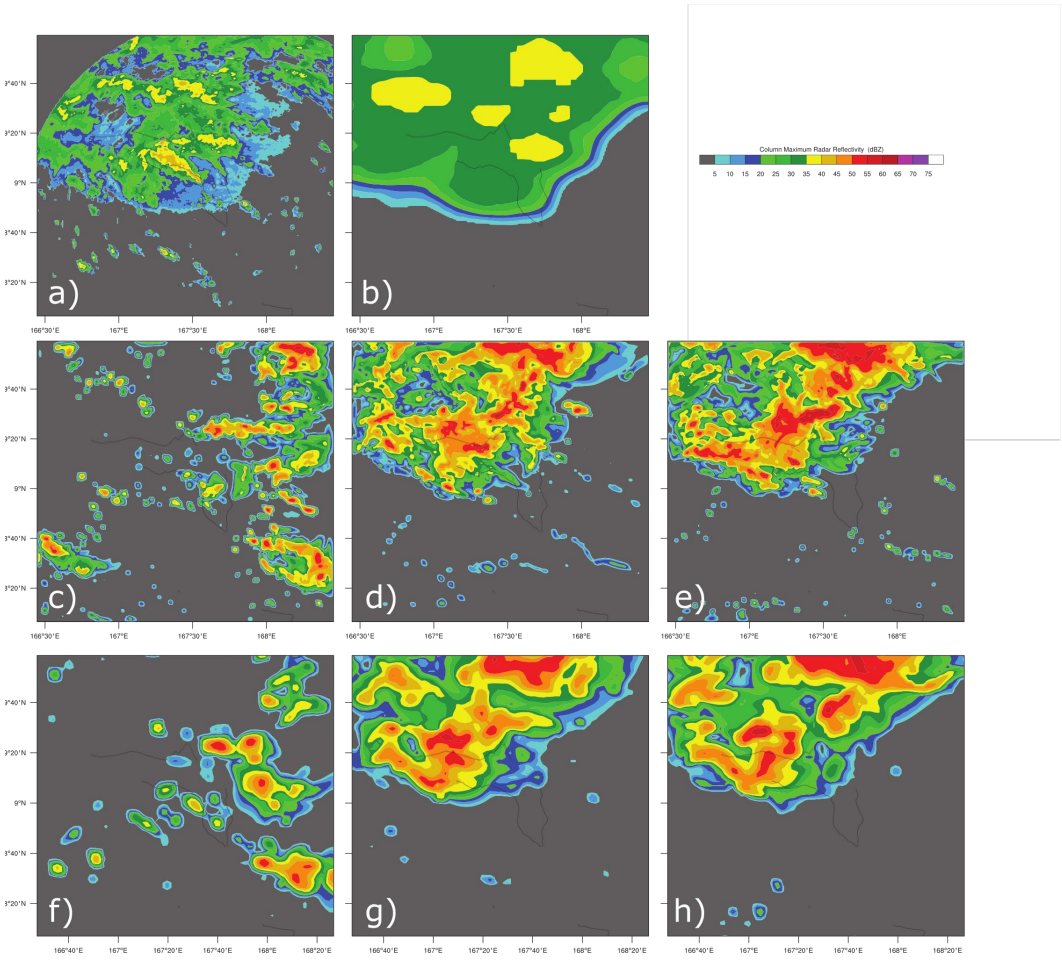

Fig. 9 CMR at end of preforecast (1800 UTC 28 May 2020) from a) radar, b) GSWR, c) A1, d) E1, e) G1, f) A3, g) E3, and h) G3 over area of 1-km domain

For 1800 UTC on 28 May 2020 (Fig. 9) the GSWR (Fig. 9b) again generally seems to be a smoothed version of the radar (Fig. 9a). Here, it is clear that in addition to GSWR being unable to resolve the details within the large area of non-negligible CMR, it also misses smaller convective elements altogether (e.g., those seen in the southern third of the domain in the radar). The area in the northwestern corner of the domain where radar data are not available is clearly seen in Fig. 9a. The use of GSWR assimilation improves the coverage and placement of convection (Fig. 9d

and e vs. c, and g and h vs. f). GSWR assimilation Methodology G allows stronger small convection to occur in the 1-km Detailed configuration (G1 in Fig. 9e vs. E1 in Fig. 9d). Experiment G thus allows the model to communicate that small areas of convection may occur, even though it is difficult to correctly place them, rather than using GSWR data to suppress small convection that may exist but just be too small for GSWR to resolve.

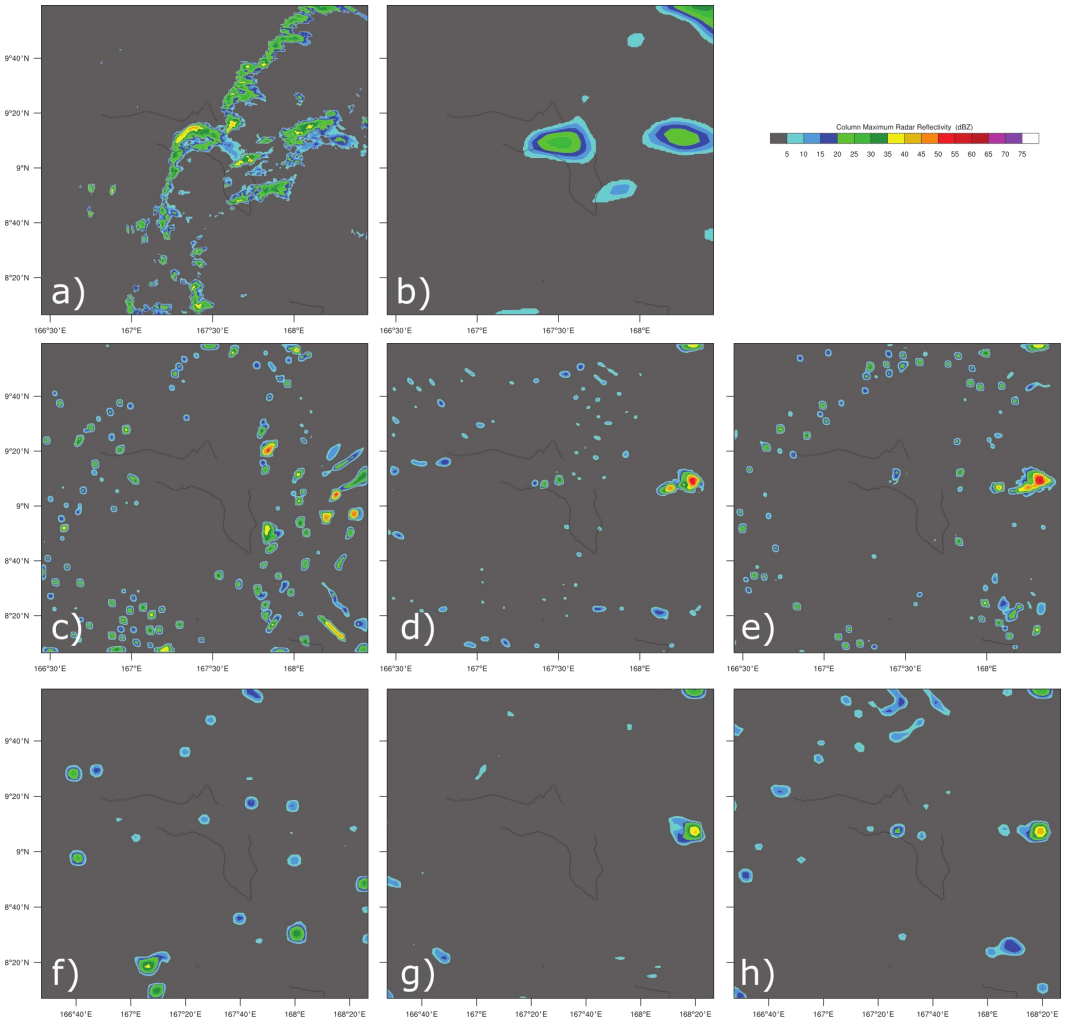

Fig. 10 CMR at end of preforecast (0400 UTC 8 June 2020) from a) radar, b) GSWR, c) A1, d) E1, e) G1, f) A3, g) E3, and h) G3 over area of 1-km domain

For 0400 UTC on 8 June 2020 (Fig. 10) more of the convection is small scale (Fig. 10a) than in previously discussed cases; so, GSWR (Fig. 10b) misses more of the first-order structure of the convection (e.g., the line aligned south–southwest to north–northeast in the northern half of the domain). While assimilation of GSWR allowed the area of convection along the middle of the eastern edge to be included in WRF, it was not as effective at reproducing the element GSWR showed just to the west of this. In addition, WRF did not represent the SSW-to-NNE line seen in

the radar but not represented in GSWR. The use of Methodology G seemed to do better in representing the overall coverage of reflectivity than Methodology E due to it not allowing GSWR to suppress small convection.

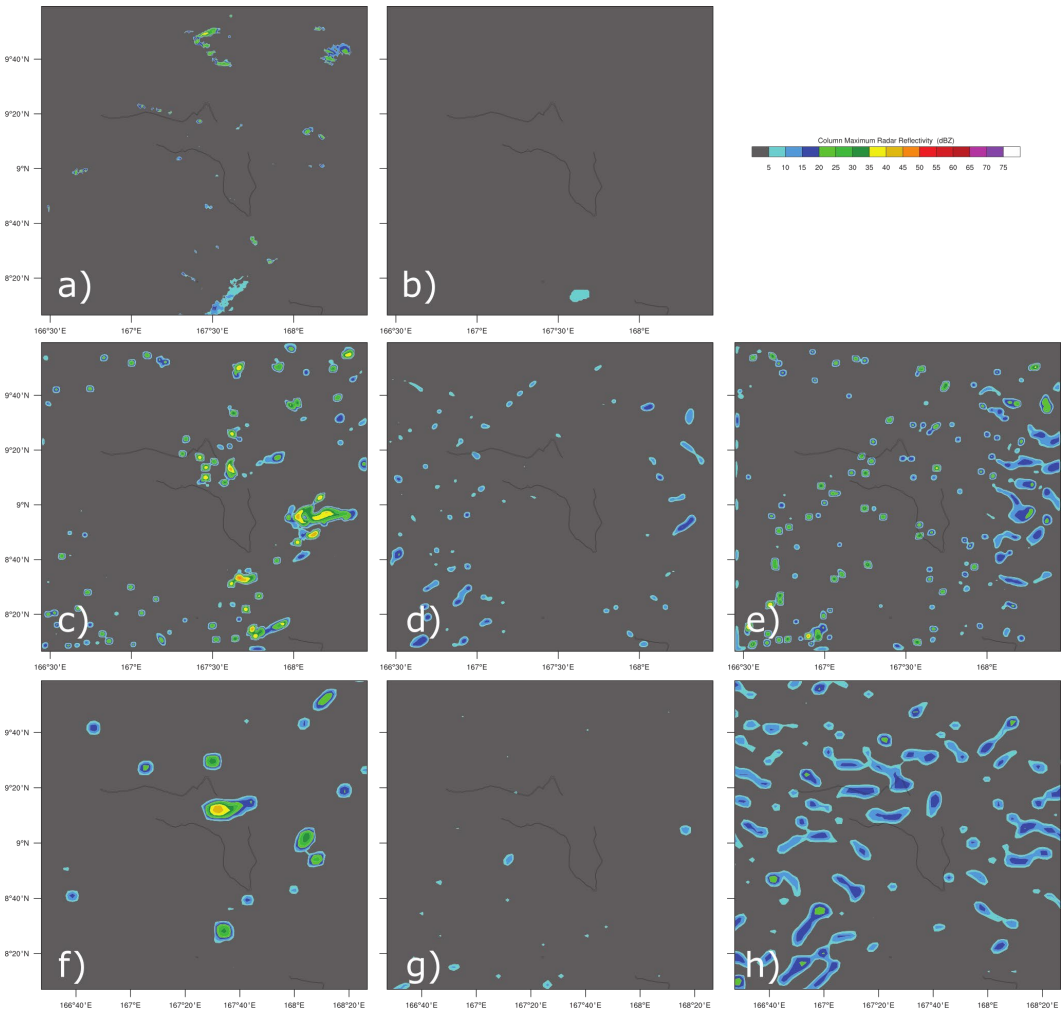

Fig. 11 CMR at end of preforecast (1800 UTC 10 June 2020) from a) radar, b) GSWR, c) A1, d) E1, e) G1, f) A3, g) E3, and h) G3 over area of 1-km domain

For 1800 UTC on 10 June 2020 (Fig. 11) only small-scale convection was indicated by radar (Fig. 11a) and GSWR (Fig. 11b) only indicated one very small area of weak CMR. While assimilation of GSWR allowed for suppression of convection in the control experiment (Fig. 11d vs. c, and g vs. f) that was not seen in radar data, preventing GSWR from suppressing small convection led to too-widespread CMR (Fig. 11e and h). In this case the relative coarseness of the GSWR data compared with radar data limits the value GSWR can provide.

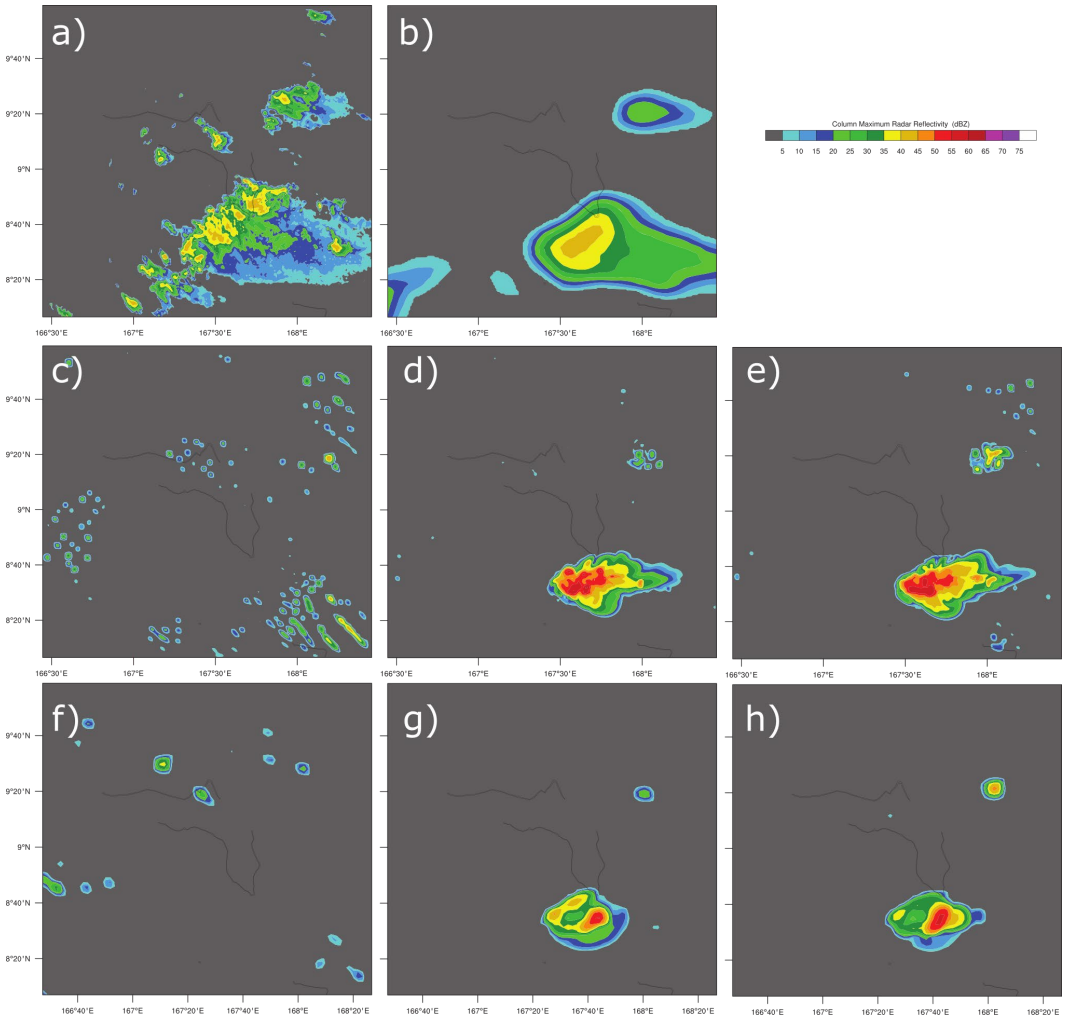

Fig. 12 CMR at end of preforecast (0800 UTC 11 June 2020) from a) radar, b) GSWR, c) A1, d) E1, e) G1, f) A3, g) E3, and h) G3 over area of 1-km domain

At 0800 UTC on 11 June 2020 there are two main areas of CMR in radar (Fig. 12a), with one larger and more southern than the other, and these are represented in GSWR (Fig. 12b) while some smaller areas are not. Assimilation of GSWR allows WRF to place reflectivity in the areas of these two main areas of CMR (Fig. 12d, e, g, and h). The area covered by the southern and larger area of convection is not as large in WRF as indicated by radar or GSWR. Preventing the GSWR data from suppressing small-scale convection in Methodology G (Fig. 12e and h) allows the northern area to be larger and more robust (than in Methodology E; Fig. 12d and g), consistent with radar. The prevention of small-scale convection suppression by GSWR appears to have allowed the more accurate development of this convective element.

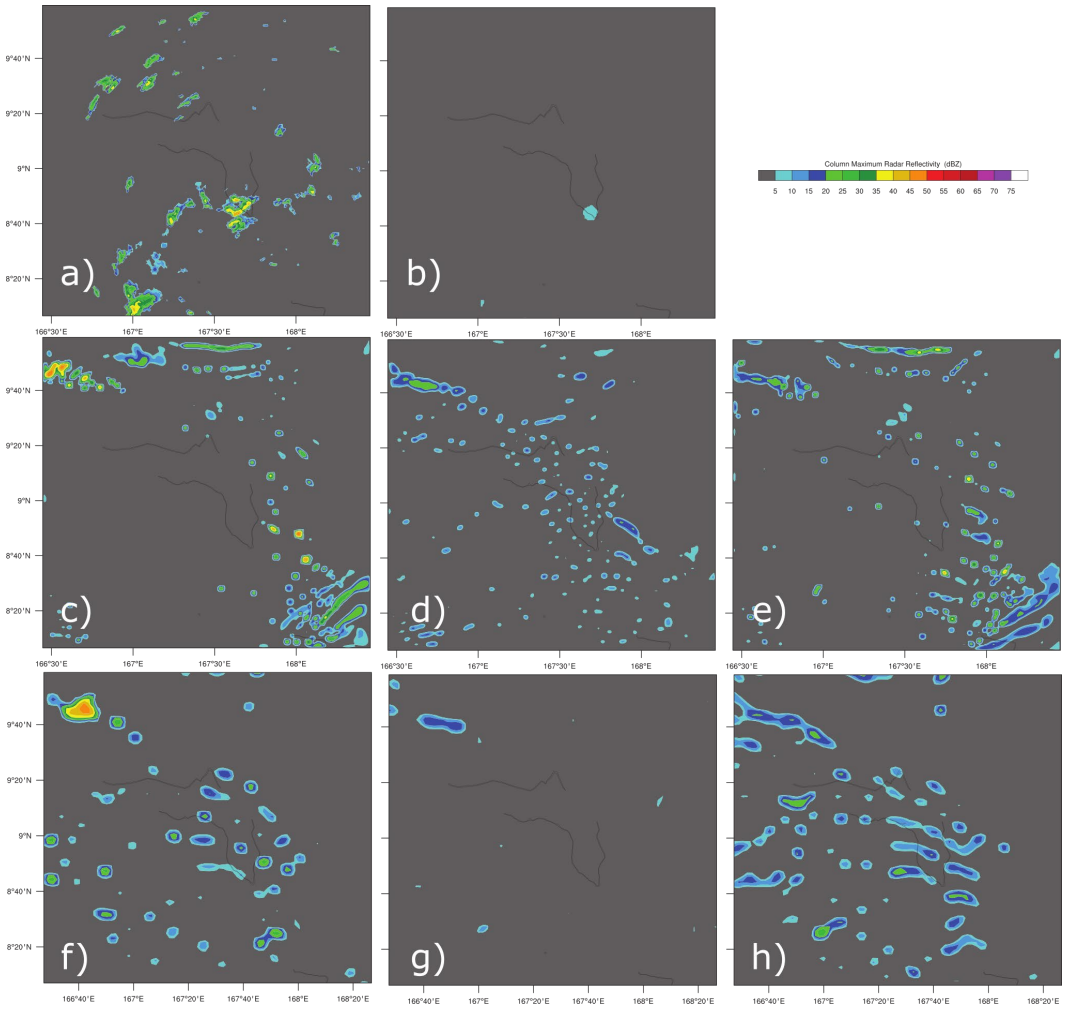

Fig. 13 CMR at end of preforecast (0600 UTC 13 June 2020) from a) radar, b) GSWR, c) A1, d) E1, e) G1, f) A3, g) E3, and h) G3 over area of 1-km domain

GSWR showed very little (Fig. 13b) at 0600 UTC on 13 June 2020, as the convection seen by radar (Fig. 13a) was apparently too small to be resolved by GSWR. Thus, assimilation of GSWR removed some of the convection in the control experiment (Fig. 13d vs. c, and g vs. f), although in the Detailed configuration seems to have resulted in more widespread, very weak CMR (Fig. 13d vs. c). Preventing GSWR suppression of small-scale convection allowed experiments with GSWR assimilation to have stronger small-scale convection in the Detailed (Fig. 13e vs. d) and Fast configuration (Fig. 13h vs. g) and much more widespread, small-scale convection in the Fast configuration. Thus, preventing GSWR from suppressing small-scale convection may allow the initial conditions to better account for the fact that convection may be occurring even though GSWR does indicate it is occurring.

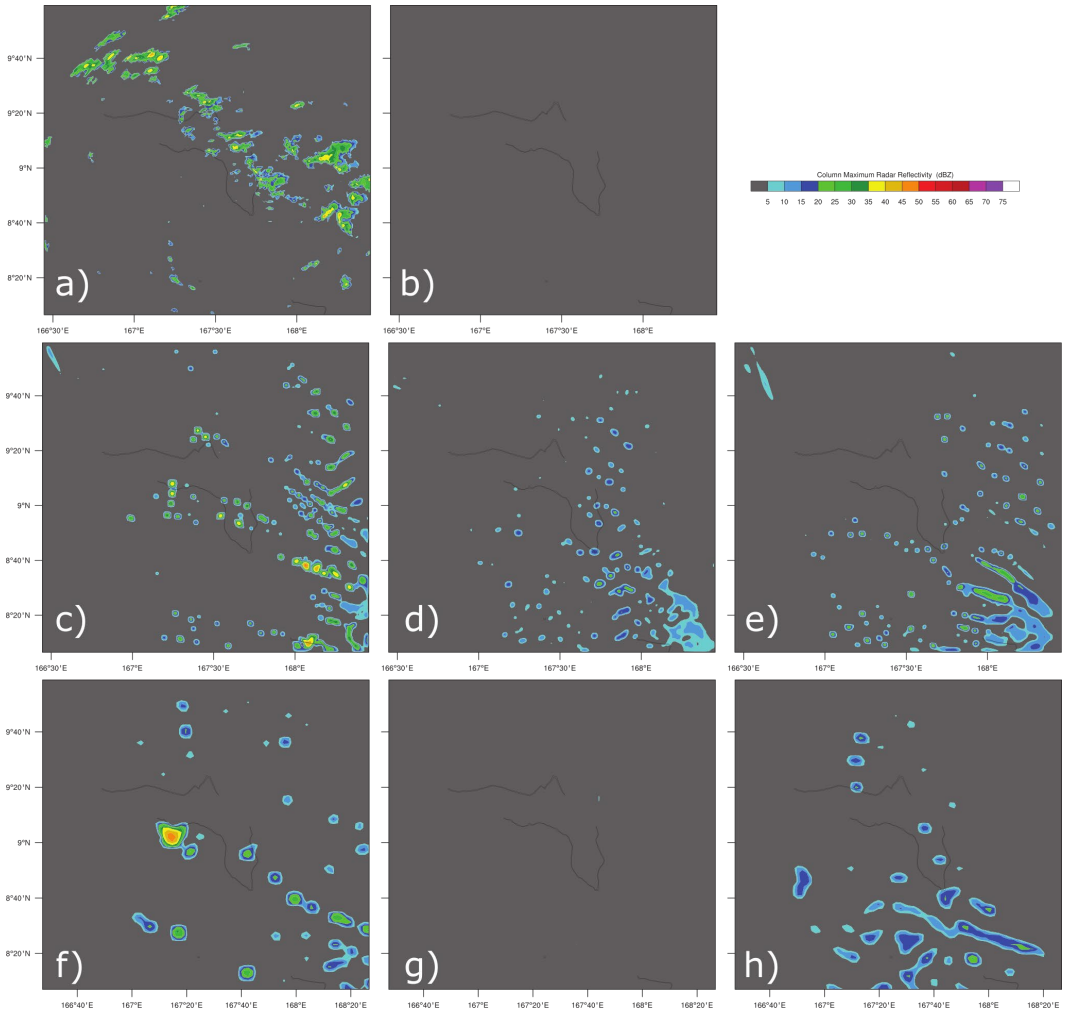

Fig. 14 CMR at end of preforecast (1800 UTC 19 June 2020) from a) radar, b) GSWR, c) A1, d) E1, e) G1, f) A3, g) E3, and h) G3 over area of 1-km domain

The final case days are shown in Fig. 14, and this is a case where even though there is non-negligible convection occurring (Fig. 14a), the individual elements are apparently too small for GSWR to detect or are missed by GSWR for some other reason (Fig. 14b). Therefore, assimilation of GSWR damps the convection in the control experiment (Fig. 14d vs. c, and g vs. f). Preventing GSWR suppression of small-scale convection allows for additional areas with non-negligible CMR (Fig. 14e vs. d, and h vs. h), which is more consistent with the radar observations; however, the strength, locations, and so on of the non-negligible CMR are not consistent with the radar observations.

The examination of the 0-h forecast of the seven case days indicates that GSWR is beneficial in improving the 0-h forecast when the convective elements are large enough to be resolved by GSWR. Limiting the ability of GSWR to suppress small-

scale convection appears generally beneficial toward providing a better representation of the coverage of small convective elements. The Fast configuration provides a smoother representation of CMR than the Detailed configuration, which is consistent with the difference in the horizontal grid spacings of the two configurations. However, other than this there was not clear evidence that either the Detailed or Fast configuration provided an overall better representation of the true atmosphere as approximated by the radar.

4. Summary and Conclusions

This study enhanced the GSWR assimilation methodology described in Reen et al. (2020), evaluated results against radar (rather than against GSWR itself as in Reen et al. [2020]), and then carried out experiments to determine details on how to best use GSWR assimilation. The details investigated included which variant of the GSWR assimilation methodology should be used and whether a high-resolution, slower, Detailed configuration provides sufficient improvement to be used instead of the lower-resolution but faster Fast configuration.

Three case days were run using the Detailed configuration and used to evaluate which of six GSWR assimilation methodologies should be used. The FSS and bias scores of this configuration indicated clear value in assimilating GSWR and were used to choose two methodologies to apply in further testing. Both methodologies chosen for further evaluation use a technique introduced here wherein GSWR data are not permitted to weaken convection in a location where GSWR data indicate that there is non-negligible reflectivity. The two methodologies chosen (E and G) differ in that one of them (G) does not allow GSWR to suppress convection where GSWR indicates negligible reflectivity if the convection is less than 9-km in horizontal extent. This is implemented because small areas of convection may exist but be too small for GSWR to resolve, and thus the absence of a small area of convection in GSWR should not be used to suppress these small areas of convection.

Seven case days were run using both the Detailed and Fast configurations to evaluate the two GSWR assimilation methodologies chosen using the three case days. The seven case days confirmed that GSWR assimilation results in clear improvement to WRF reflectivity forecasts. In terms of FSS, this benefit lasted throughout the 6-h forecast at the 10-dBZ threshold, 4 h at the 20-dBZ threshold, and 3 h at the 30-dBZ threshold. GSWR assimilation improved an underforecast bias at the 10- and 20-dBZ thresholds, especially with Methodology G, while at the 30-dBZ threshold GSWR assimilation caused on overforecast bias, particularly for Methodology G. However, the 30-dBZ threshold covers less area than the lower

thresholds and so better bias at the two lower thresholds seems preferable to better bias at the higher threshold. Overall, the assimilation Methodologies E and G performed similarly but G seemed slightly better and so was chosen for future work. The Detailed and Fast configurations seemed to produce very similar verification scores, so the verification scores did not support using the Detailed configuration, given the much higher computational cost. Examination of the 0-h forecast CMR for each of the seven case days indicates that GSWR provides value in the cases where convective elements are large enough to be resolved by GSWR.

Based on the evaluation in this study, we recommend assimilating GSWR data via Methodology G while using the Fast configuration. It is suspected there is benefit to using the higher-resolution Detailed configuration, as it should produce more realistic horizontal and vertical convective structure. However, given that the Detailed configuration runs much more slowly (about nine times as slow in testing), use of the Detailed configuration may require much longer intervals among cycles, which will likely degrade forecast results significantly. The field being assimilated here (GSWR) is coarser than the finest domains in either configuration (horizontal grid spacing of 5 km in GSWR compared with 1 km in Detailed and 3 km in Fast). Thus, different results on the relative value of the Detailed versus Fast configuration might be found if a higher-resolution data source such as radar were being assimilated.

Assimilation of GSWR can improve NWP forecasts of convection and has the advantage of providing near-global coverage but also the disadvantage that it cannot resolve small-scale convection. Where radar data are available it is better to assimilate radar data since that is a more direct measurement, provides higher spatial and temporal resolution, and resolves vertical variability. Because the GSWR data do not resolve fine-scale convection, future work should investigate other alternatives to radar that cover large areas and provide observations with high spatial resolution and high temporal resolution that can be used to improve WRF moist-convection forecasts. Satellite-derived observations such as cloud-top temperature tendency, cloud-top height, and rain rate from the Himawari satellite or GOES satellites may better resolve fields important for forecasting small-scale convection than the current 5-km GSWR. Since the GSWR algorithm provides a mechanism to combine data from multiple sources including GOES and Himawari to create radar-like fields, the best solution may be if GSWR were enhanced to be at higher resolution and include ingestion of high-resolution satellite data and then this enhanced GSWR was assimilated into WRF.

5. References

Alexander C, Dowell D, Hu M, Ladwig T, Weygandt S, Benjamin SG. Expanding use of radar data in deterministic and ensemble data assimilation for the High-Resolution Rapid Refresh (HRRR). Presented at 38th Conference on Radar Meteorology; American Meteorological Society; 2017 Aug 28–Sep 1; Chicago, IL. 19B.2. c2017. https://ams.confex.com/ams/38RADAR/webprogram/Paper321169.html.

Benjamin SG, Weygandt S, Brown JM, Hu M, Alexander CR, Smirnova TG, Olson JB, James EP, Dowell DC, Grell GA, et al. A North American hourly assimilation and model forecast cycle: the rapid refresh. Mon Weather Rev. 2016;144(4):669–1694.

Hong S, Lim J. The WRF single-moment 6-class microphysics scheme (WSM6). J Korean Meteorol Soc. 2006;42(2):129–151.

Hong, S, Noh, Y, Dudhia, J. A new vertical diffusion package with an explicit treatment of entrainment processes. Mon Wea Rev. 2006:134(9): 2318–2341.

Iacono MJ, Delamere JS, Mlawer EJ, Shephard MW, Clough SA, Collins WD. Radiative forcing by long-lived greenhouse gases: calculations with the AER radiative transfer models. J Geophys Res. 2008;113:D13103.

Jimenez PA, Dudhia J, Gonzalez–Rouco JF, Navarro J, Montavez JP, Garcia–Bustamante E. A revised scheme for the WRF surface layer formulation. Mon Weather Rev. 2012;140:898–918.

[NCEP] National Centers for Environmental Prediction/National Weather Service/NOAA/US Department of Commerce. NCEP GFS 0.25 degree global forecast grids historical archive. Research Data Archive at the National Center for Atmospheric Research, Computational and Information Systems Laboratory; 2015. https://doi.org/10.5065/D65D8PWK.

Reen BP, Dawson LP. The Weather Running Estimate–Nowcast Realtime (WREN_RT) system, version 1.03. Army Research Laboratory (US); 2018 Sep. Report No.: ARL-TR-8533. https://apps.dtic.mil/sti/pdfs/AD1060869.pdf.

Reen BP, Cai H, Raby JW. Radar assimilation over Kwajalein Atoll. CCDC Army Research Laboratory (US); 2019 Oct. Report No.: ARL-TR-8831. https://apps.dtic.mil/sti/pdfs/AD1082516.pdf.

Reen BP, Cai H, Raby JW. Preliminary investigation of assimilating Global Synthetic Weather Radar. CCDC Army Research Laboratory (US); 2020 Sep. Report No.: ARL-TR-9072. https://apps.dtic.mil/sti/pdfs/AD1111072.pdf.

Roberts N. Assessing the spatial and temporal variation in the skill of precipitation forecasts from an NWP model. Meteor Appl. 2008;15:163–169.

Roberts N, Lean H. Scale-selective verification of rainfall accumulations from high-resolution forecasts of convective events. Mon Wea Rev. 2008;136:78–97.

Shao H, Derber J, Huang XY, Hu M, Newman K, Stark D, Lueken M, Zhou C, Nance L, Kuo YH, Brown B. Bridging research to operations transitions: status and plans of community GSI. B Am Meteorol Soc. 2016;97:1427–1440.

Skamarock WC, Klemp JB, Dudhia J, Gill DO, Liu Z, Berner J, Wang W, Powers JG, Duda MG, Barker DM, et al. A description of the advanced research WRF model version 4. National Center for Atmospheric Research; 2019. Report No.: NCAR/TN-556+STR.

Tewari M, Chen F, Wang W, Dudhia J, LeMone MA, Mitchell K, Ek M, Gayno G, Wegiel J, Cuenca RH. Implementation and verification of the unified NOAH land surface model in the WRF model. In: 20th Conference on Weather Analysis and Forecasting/16th Conference on Numerical Weather Prediction; 2004 Jan 12–16; Seattle, WA. American Meteorological Society. c2004. p. 11–15.

Veillette MS, Hassey EP, Mattioli CJ, Iskenderian H, Lamey PM. Creating synthetic radar imagery using convolutional neural networks. J Atmos Oceanic Technol. 2018:35(12):2328–2338.

Veillette MS, Iskenderian H, Lamey PM, Mattioli CJ, Banerjee A, Worris M, Porschitsky AB, Ferris RF, Manwelyan A, Rajagoplalan S, et al. Global synthetic weather radar in AWS GovCloud for the U.S. Air Force. Presented at 19th Conference on Artificial Intelligence for Environmental Science; American Meteorological Society; 2020 Jan 13–16; Boston, MA. J69.3. https://ams.confex.com/ams/2020Annual/meetingapp.cgi/Paper/363150.

Zhang C, Wang Y. Projected future changes of tropical cyclone activity over the western North and South Pacific in a 20-km-mesh regional climate model. J Climate. 2017;30:5923–5941.

List of Symbols, Abbreviations, and Acronyms

CMR	column maximum reflectivity
CPHT	cumulus parameterization heating term
FSS	fractions skill score
GFS	Global Forecast System
GOES	Geostationary Operational Environment Satellite
GSI	Gridpoint Statistical Interpolation
GSWR	Global Synthetic Weather Radar
MADIS	Meteorological Assimilation Data Ingest System
MIT-LL	Massachusetts Institute of Technology–Lincoln Laboratory
MM5	Pennsylvania State University–NCAR Mesoscale Model version 5
MPHT	microphysics heating term
NASA	National Aeronautics and Space Administration
NCAR	National Center for Atmospheric Research
NSST	Near-Surface Sea Temperature
NWP	numerical weather prediction
RDLH	reflectivity-derived latent heating
RRTMG	Rapid Radiative Transfer Model for General circulation models
RTG	Realtime Global
UTC	coordinated universal time
WREN_RT	Weather Running Estimate–Nowcast Realtime system
WRF	Weather Research and Forecasting model
WRF-ARW	Advanced Research version of the Weather Research and Forecasting model

1 (PDF)	DEFENSE TECHNICAL INFORMATION CTR DTIC OCA
1 (PDF)	DEVCOM ARL FCDD RLD DCI TECH LIB
3 (PDF)	DEVCOM ARL FCDD RLC EM H CAI J RABY B REEN